



HAL
open science

Determining singular and non-singular Williams' expansion terms from full-field measurements: consideration of structural effects on fracture behaviour

Bastien Lammens, Gérald Portemont, Julien Berthe, Rian Seghir, Julien Réthoré

► To cite this version:

Bastien Lammens, Gérald Portemont, Julien Berthe, Rian Seghir, Julien Réthoré. Determining singular and non-singular Williams' expansion terms from full-field measurements: consideration of structural effects on fracture behaviour. *Theoretical and Applied Fracture Mechanics*, 2024, 130 (104304), 10.1016/j.tafmec.2024.104304 . hal-04446229v2

HAL Id: hal-04446229

<https://hal.science/hal-04446229v2>

Submitted on 29 May 2024

HAL is a multi-disciplinary open access archive for the deposit and dissemination of scientific research documents, whether they are published or not. The documents may come from teaching and research institutions in France or abroad, or from public or private research centers.

L'archive ouverte pluridisciplinaire **HAL**, est destinée au dépôt et à la diffusion de documents scientifiques de niveau recherche, publiés ou non, émanant des établissements d'enseignement et de recherche français ou étrangers, des laboratoires publics ou privés.

Determining singular and non-singular Williams' expansion terms from full-field measurements: consideration of structural effects on fracture behaviour

Bastien Lammens^{a,b,*}, Gérald Portemont^a, Julien Berthe^a, Rian Seghir^b, Julien Réthoré^b

^a*DMAS, ONERA, F-59014 Lille-France*

^b*Nantes Université, Ecole Centrale Nantes, CNRS, GeM, UMR 6183, 1 rue de la Noë, France*

Abstract

When a cohesive crack propagates within a fibre reinforced composite, the crack tip will potentially be subjected to complex far-field stress. In quasi-brittle or ductile materials, the latter may affect the fracture behaviour itself hence predictions simply using Griffith theory may deviate from experience. In this context, we investigated the influence of higher order linear elastic fracture mechanics parameters T and B (translating the nature of far-field stress) on K_{IC} during mode I crack propagation. Full-field measurements are considered using both Digital Image Correlation (DIC) and Williams' series expansion to obtain K_{IC} , T and B . The objective is to determine K_{IC} by taking into account structural effects with T and B . Metrological aspects are initially assessed to evaluate the error bars for the method when considering realistic experimental biases. In particular, the influence of the projection zone, camera sensor noise and the speckle-like DIC pattern on the evaluation of K_{IC} , T and B were investigated. Quasi-static loading fracture experiments in mode I were ultimately performed on epoxy resin (Hex-

*Corresponding author: bastien.lammens@onera.fr

ply®M21) specimens with two different geometries (Tapered Double Cantilever Beam and triangular). It was shown that non-singular terms strongly depend on specimen geometry, inducing some structural effects in the vicinity of the crack tip. The impact of these effects on estimated K_{IC} is ultimately discussed in the light of the results of the metrological assessment.

Keywords: Williams' series, Non-singular terms, Digital image correlation, Critical stress intensity factor, Epoxy resin

1. Introduction

Organic matrix laminated composites are increasingly used in the aeronautical field to decrease the weight of structures. These materials might be subjected to impacts such as bird strikes or hailstones. Damage mechanisms may arise such as matrix cracking or delamination. Delamination involves the significant decohesion of the inter-laminar environment. During delamination, the matrix (a resin) can fail due to a cohesive fracture or an adhesive fracture [1]. This study will focus on cohesive fracture. In this context, the crack propagates into an inter-laminar layer confined by the fibres leading to constraint effects. Constraint effects is a generic term suggesting that the stress field surrounding the crack tip is not fully defined by the usual K-dominant stress field. Indeed, it can be enriched/constrained by *e.g.* the effect of free edges, stiffeners or any other stress field modifications induced by structural effects. It has been shown in the literature [2–11] (see below for more details 2) that these constraint effects may change the fracture response of the material. The critical stress intensity factor for non-ideal (perfectly brittle) material may depend on the surrounding stress field and differ from the value determined in standardized experiments. One way to vary these constraint effects during an experimental campaign is to change the specimen geometry.

The consequences of these constraint effects on the fracture response of a material can be evaluated using different methods according to the literature. Two types of approach can be used, a macroscopic approach with global measurements and a microscopic approach with local measurements. One global approach, the R-curve (or crack growth resistance curve), can be used to study variation in crack

growth resistance G_R or the stress intensity factor K_I or the energy release rate G versus crack extension a . A series of authors [12–14] observed that the latter is influenced by the geometry of the specimen. However, although geometrical effects have been highlighted, the dependence of the stress fields on the specimens considered leading to different values of K_{IC} or G_{IC} has not been taking into account.

Based on these observations, a more descriptive approach can be used considering stress field criteria *e.g.* based on K_I , T and B . T or $T - stress$ (first non-singular term) and B or $B - stress$ (second non-singular term) are the higher order terms in the Williams' series. The Williams' expansion involves a series of analytical solutions for the displacement, strain and stress fields near the crack tip for a 2D elastic body with a semi-infinite straight crack [15]. These non-singular terms can be used to determine the constraint effects and their influence on K_{IC} [2–11]. Some of these authors have used numerical simulation configured with the experimental fracture load to obtain K_{IC} , T and B and to determine a relationship between K_{IC} and the non-singular terms (more details in section 2) [2, 7, 9–11, 16]. However, all of the above approaches require numerical or semi-analytical complements as well as global measurements, which are potentially biased due to the consideration of ideal loading conditions.

Digital Image Correlation (DIC) offers a very promising method for the accurate identification of T and B as the basis for a microscopic approach. Indeed, full-field imaging techniques are more commonly used because they can capture the full complexity of the displacement field around the crack [17–22]. Subset-based DIC [23, 24] or FE-based DIC are the most common [25, 26] strategies. Williams' series can be used with displacement fields obtained from DIC to iden-

tify the apparent position of the elastic crack tip [18, 19], with sub-pixel precision, but also K_{IC} and higher order terms, such as T or B [19, 20, 22, 27, 28].

In this paper, the aim is to determine K_{IC} while considering structural effects. More specifically, the paper focuses on the systematic relationship between structural or geometrical effects and non-singular terms T and B as well as K_{IC} . Full-field imaging techniques based on DIC, associated with the Williams' series expansion are used to investigate the aforementioned effects. Crack initiation is beyond the scope of this study, only crack propagation is considered.

The paper is divided into three parts. The first part considers the literature and some analytical developments to illustrate the influence of the non-singular term on K_{IC} . The second part presents the numerical method used to determine K_{IC} , T and B by projecting the displacement fields obtained from DIC onto the Williams' series. Metrological aspects of synthetic data are analyzed (artificially deformed images). Close attention is paid to the robustness of the identification of Williams' series terms with respect to camera noise, the projection zone and speckle pattern variation. The third part describes quasi-static mode I fracture experiments on Hexply®M21 epoxy resin with two specific geometries (TDCB and triangular, see 8 for details) and the analysis of variations in K_I , T and B during crack propagation. Finally, considering that the Griffith criterion still holds in the presence of strong constraint effects, *i.e.* that the crack propagates at $G_I = G_{IC}$, the equivalence between G_{IC} and K_{IC} , *e.g.* corresponding to Irwin's relationship ($G_{IC} = \frac{K_{IC}^2}{E}$) also remains valid. On this basis, in this paper, the crack is assumed to propagate at $K_I = K_{IC}$ which allows a parametric relationship to be deter-

mined between K_{IC} , T and B .

2. Non-singular terms and constraint effects

The non-singular terms T and B will be used in this paper to describe the constraint effects. The stress equation obtained from the Williams' series (equation 1) taking into account higher order terms T and B is considered to reflect their influence on K_{IC} . Indeed, modifying the geometry of the specimen will modify the stress field around the crack tip, changing the values of T and B for a given value of K_I . According to equation 1, the contribution of K_I , T and B respectively to the stress field, scales to $r^{-1/2}$, r^0 and $r^{1/2}$ respectively, which means that near the crack tip, *e.g.* $r \approx 10 \mu\text{m}$, K_I is dominant compared to T and B . However, from a specific distance to the crack tip, $r \approx 100 \mu\text{m}$ for example, the contribution of K_I may decrease while that of the non-singular terms can increase. This illustrates the role of far-field stress T and B .

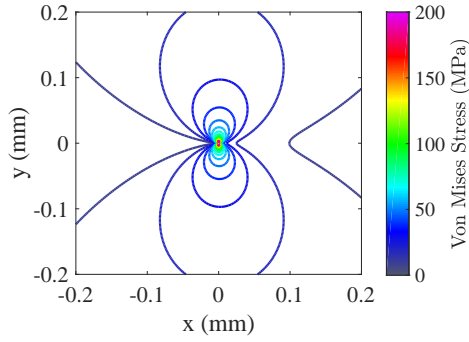
Kumar *et al.* determined the degree of K_I dominance for different specimens [9]. For a Single Edge Notch Tension (SENT) specimen ($C > 1.5 \text{ mm}^{-1}$ in Figure 2b), the authors showed that for $r > 150 \mu\text{m}$, the non-singular terms contribute more than 10 %. These terms naturally reflect the main characteristics of the far-field stress induced by various specimen geometries; T describes the effect of a homogeneous stress parallel to the crack direction, while B describes the presence of an opening stress field modifying the crack opening profile. Both the intensity of the stress field and field variation around the crack tip are affected by these terms. Bouledroua *et al.* showed that the plastic area is oriented in the same

direction as crack extension for $T > 0$ and in the opposite direction for $T < 0$ [4]. This remark is illustrated in Figure 1. Indeed, the shape and values of the stress fields differ according to the values of T and B . In Figure 1b, the iso-contour of the Von Mises stress oriented in the opposite direction to the crack extension while it is oriented in the same direction as crack extension in Figures 1c to 1e. In these Figures, three values of B are considered, which modify the values of the stress fields with almost the same shape as the iso-contour of the Von Mises stress.

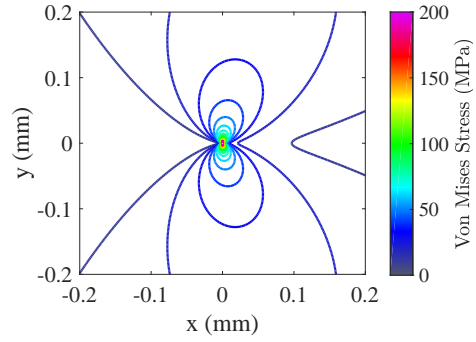
$$\begin{pmatrix} \sigma_x \\ \sigma_y \\ \sigma_{xy} \end{pmatrix} = \begin{pmatrix} \frac{1}{4} \frac{K_I}{\sqrt{2\pi r}} [3\cos(\frac{\theta}{2}) + \cos(\frac{5\theta}{2})] + T + \frac{3}{4} \frac{B\sqrt{r}}{\sqrt{2\pi}} [5\cos(\frac{\theta}{2}) - \cos(\frac{3\theta}{2})] \\ \frac{1}{4} \frac{K_I}{\sqrt{2\pi r}} [5\cos(\frac{\theta}{2}) - \cos(\frac{5\theta}{2})] + \frac{3}{4} \frac{B\sqrt{r}}{\sqrt{2\pi}} [3\cos(\frac{\theta}{2}) + \cos(\frac{3\theta}{2})] \\ \frac{1}{4} \frac{K_I}{\sqrt{2\pi r}} [\sin(\frac{5\theta}{2}) - \sin(\frac{\theta}{2})] - \frac{3}{4} \frac{B\sqrt{r}}{\sqrt{2\pi}} [\sin(\frac{3\theta}{2}) + \sin(\frac{\theta}{2})] \end{pmatrix} \quad (1)$$

In terms of crack behaviour, Cotterell explained that B controls the stability of crack propagation (*i.e.* if the crack propagates in a stable or unstable manner) and T controls the stability of the direction of cracking [6]. Other authors have shown that crack orientation may depend on T [2–8, 29] under mode I loading.

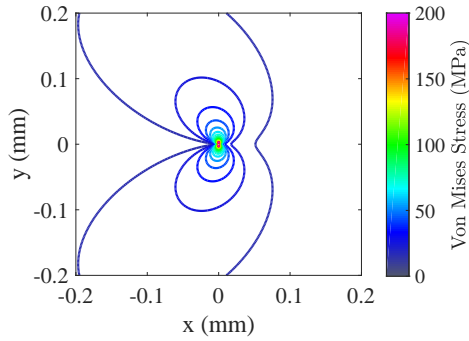
Other authors have studied the influence of T and B on K_{IC} . Chao *et al.* determined K_{IC} for PMMA specimens using a numerical procedure and the fracture load following ASTM E399-92 guidelines [10, 11, 30]. By defining two criteria, they identified the two non-singular terms T and B . They then showed a decrease in K_{IC} with B and an increase in K_{IC} with T . A similar approach was also used by Kumar *et al.* on PMMA specimens [9]. The critical energy release rate G_{IC} was evaluated using a finite element model and the measured fracture load. Then, K_{IC} was obtained using a classical formulation assuming pure plain strain mode I opening *i.e.* $G_{IC} = \frac{K_{IC}(1-\nu^2)}{E}$. They showed that K_{IC} depends on the geometry



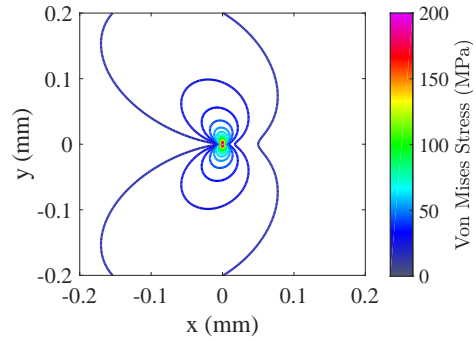
(a) $K_I = 1 \text{ MPa m}^{\frac{1}{2}}$ $T = 0 \text{ MPa}$ $B = 0 \text{ MPa m}^{-\frac{1}{2}}$



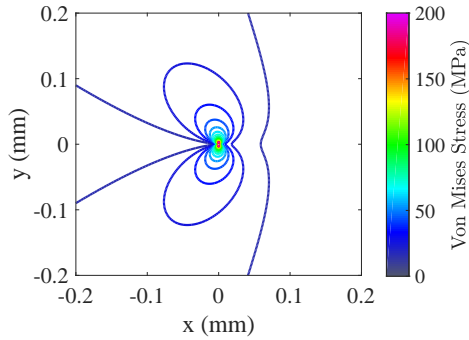
(b) $K_I = 1 \text{ MPa m}^{\frac{1}{2}}$ $T = -10 \text{ MPa}$ $B = 0 \text{ MPa m}^{-\frac{1}{2}}$



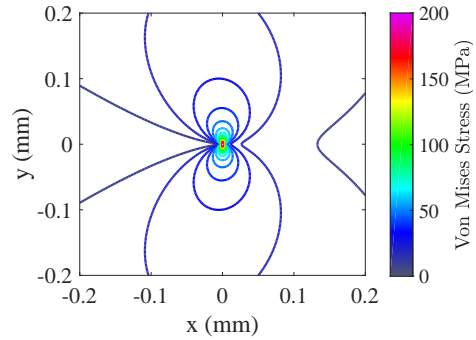
(c) $K_I = 1 \text{ MPa m}^{\frac{1}{2}}$ $T = 10 \text{ MPa}$ $B = 0 \text{ MPa m}^{-\frac{1}{2}}$



(d) $K_I = 1 \text{ MPa m}^{\frac{1}{2}}$ $T = 10 \text{ MPa}$ $B = -100 \text{ MPa m}^{-\frac{1}{2}}$



(e) $K_I = 1 \text{ MPa m}^{\frac{1}{2}}$ $T = 10 \text{ MPa}$ $B = 400 \text{ MPa m}^{-\frac{1}{2}}$



(f) $K_I = 1 \text{ MPa m}^{\frac{1}{2}}$ $T = 0 \text{ MPa}$ $B = 400 \text{ MPa m}^{-\frac{1}{2}}$

Figure 1: Analytical Von Mises stress field (from equation 1) for different values of K_I , T and B
: Influence of T and B on the stress field

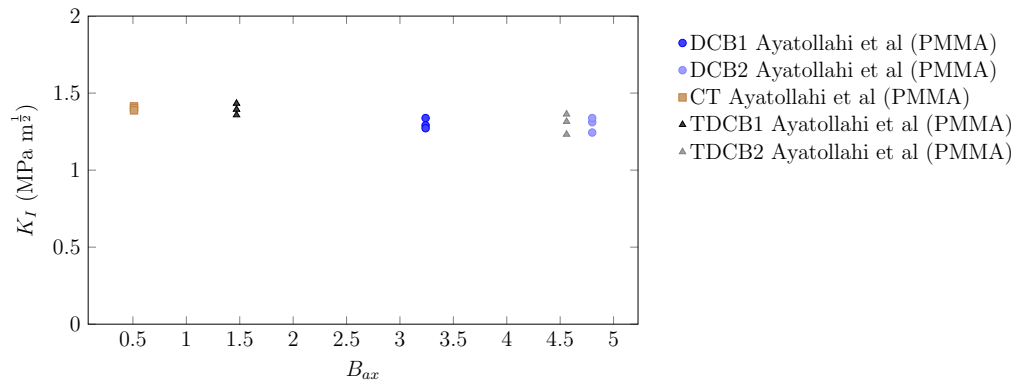
of the specimen under consideration.

However, as the physical implications of the higher orders T and B are difficult to understand, some authors favored the biaxiality ratio, B_{ax} , instead of T and a C coefficient instead of B . B_{ax} is defined, in mode I , as follows:

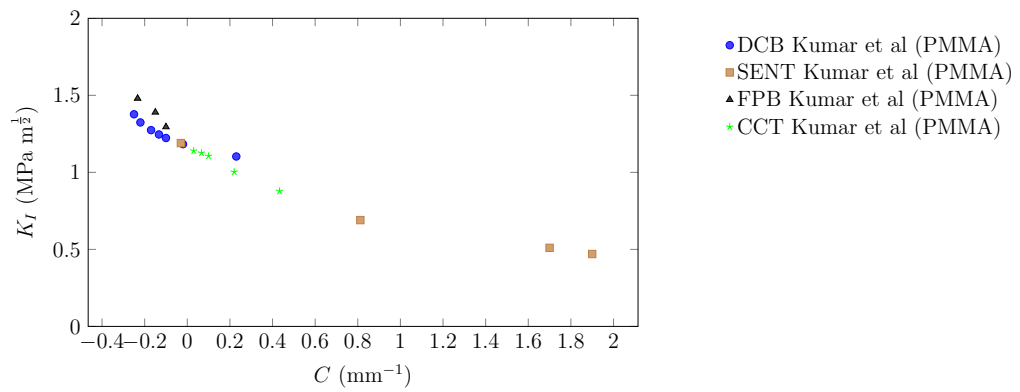
$$B_{ax} = \frac{T\sqrt{\pi a}}{K_I} \quad (2)$$

where a is the crack length. Using this definition, B_{ax} is the biaxiality coefficient or stress biaxiality ratio at infinity, *i.e.* ratio of the stress in the x direction to the stress in the y direction at infinity. Using this framework, Ayatollahi *et al.* and Razavi *et al.* [2, 7] highlighted an increase in the biaxiality ratio when the crack deviates whereas it remains constant if the crack remains on the original crack path. These authors also showed that the ratio depends on the specimen considered and K_{IC} (considered as apparent in their works) decreases with respect to B_{ax} for PMMA (see Figure 2a). This trend differs from the one identified by Chao *et al.* although they studied the same material [2, 10]. As an alternative to B , Kumar *et al.* considered $C = \frac{3B}{K_I}$ that can be considered as the slope of the non-singular opening profile at the crack tip. They showed that K_{IC} decreases with respect to C (see Figure 2b) [9].

In the light of the literature, the Critical Stress Intensity Factor (CSIF) cannot be considered as a constant, as it depends on the stress field, at least in some materials. Nominal CSIF noted K_{IC}^n can nevertheless still be defined as the CSIF obtained from fracture experiments where higher order terms T and B vanish, *e.g.* using the gold standard Compact Tension (CT) specimen. According to the literature, global measurements can be used to determine K_{IC} , T and B . Nevertheless,



(a)



(b)

Figure 2: Variation in K_I with respect to : (a) B_{ax} and (b) the second non-singular term C

there is still no agreement in the literature with respect to the actual relationship between K_{IC} and T or B . In this paper, full-field imaging techniques based on DIC and Williams' series are considered in order to quantitatively study the potential relationship between structural/geometrical effects, non-singular terms and K_{IC} . Moreover, to the authors' knowledge, no metrological procedure has been proposed to assess the robustness of the determination of the parameters K_I , T and B . Another potential advantage of this approach arises when considering dynamic loading. Indeed, it can prove difficult and inaccurate to measure loads, potentially leading to an incorrect evaluation of K_{IC} when using global measurements.

3. Numerical Methods

In the following paragraphs, an approach based on DIC and Williams' series is proposed to determine the stress intensity factor K_I and the non-singular terms, T and B . DIC is used to measure the displacement fields. This study uses UFreckles code [31]. A global approach based on finite element shape functions is used. The displacement fields from DIC are projected onto the Williams' series using a least squares approach to determine K_I , T and B (equations 6, 7 and 8). In a homogeneous semi-infinite elastic isotropic media, a (complex) displacement field u_w can be broken down using the Williams' series as follows [19]:

$$u_w = \sum_{j=I,II} \sum_{n=n_m}^{n_M} a_j^n \phi_j^n(z) \quad (3)$$

where a_j^n are real coefficients and ϕ_j^n are complex functions. n_m and n_M define the truncation of the Williams' series. j corresponds to the fracture modes in the plane in mode I or mode II . This truncation is classically defined between $n_m = -3$ and $n_M = 7$ which means there are eleven terms for each fracture mode [19]. And so, the truncation of the Williams' series is considered with twenty-two terms. When $n < 0$, the terms are said to be super-singular while the terms $n > 1$ are said to be non-singular. The elementary functions of the Williams' series in mode I and mode II are written as follows:

$$\phi_I^n(r, \theta) = r^{n/2} (\kappa e^{in\theta/2} - \frac{n}{2} e^{i(4-n)\theta/2} + (\frac{n}{2} + (-1)^n e^{-in\theta/2})) \quad (4)$$

$$\phi_{II}^n(r, \theta) = r^{n/2} (\kappa e^{in\theta/2} + \frac{n}{2} e^{i(4-n)\theta/2} - (\frac{n}{2} - (-1)^n e^{-in\theta/2})) \quad (5)$$

where i is a pure imaginary number, r the distance to the crack tip, and θ the angle with respect to the local reference frame aligned with the crack. κ is the Kolosov's constant, $\kappa = (3 - \nu)/(1 + \nu)$ in plane stress and $\kappa = (3 - 4\nu)$ in plane strain, and ν is the Poisson's ratio. Note that rigid body motion *i.e.* translation and rotation, are included in the Williams' series. Rigid translation correspond to the $n = 0$ and the rigid rotation is described by the $n = 2$ term for mode II [19]. The projection of the displacement fields from DIC onto the Williams' series using a least squares approach involves minimizing the discrepancy $\|LA - U\|^2$ where U is the displacement field from the DIC, A the Williams' series terms and L the projection basis with the elementary functions of the Williams' series (see table 1). This minimization leads to the use of pseudo inverse matrix of L : $(L^T L)^{-1} L^T$ to compute A as $(L^T L)^{-1} L^T U$.

$$\left| \begin{array}{c} \mathbf{L} = \begin{bmatrix} 1 & \phi_{I_1}^1 & \dots & \phi_{II_1}^n \\ \vdots & \vdots & \vdots & \vdots \\ \vdots & \vdots & \vdots & \vdots \\ 1 & \phi_{I_m}^1 & \dots & \phi_{II_m}^n \end{bmatrix} \\ \mathbf{U} = \begin{bmatrix} u_{x1} \\ \vdots \\ u_{xm} \\ u_{y1} \\ \vdots \\ u_{ym} \end{bmatrix} \\ \mathbf{A} = \begin{bmatrix} a_0 \\ \vdots \\ a_m \\ b_0 \\ \vdots \\ b_m \end{bmatrix} \end{array} \right|$$

Table 1: L, U , and A

In mode I , the stress intensity factor K_I , the first non-singular term T and the second non-singular term B are defined as :

$$K_I = \frac{E}{1 + \nu} \sqrt{2\pi} a_I^1 \quad (6)$$

$$T = \frac{4E}{1 + \nu} a_I^2 \quad (7)$$

$$B = \frac{E}{1 + \nu} \sqrt{2\pi} a_I^3 \quad (8)$$

where E is the Young's modulus. The position of the equivalent elastic crack tip is evaluated by manually defining the crack path and then using the first super-singular term $n = -1$ and the singular term $n = 1$ to iteratively correct an initial estimate as proposed by Hamam *et al.* [32]. This correction d relates to the ratio of a_I^{-1} to a_I^1 :

$$d = \frac{-2a_I^{-1}}{a_I^1}. \quad (9)$$

After convergence, when the amplitude of d is lower than 1 pixel [18, 19, 33, 34], the description obtained with the Williams' expansion best matches with

K_I^{ref}	T^{ref}	B^{ref}	$a^{ref} (x ; y)$
1 MPa m ^{$\frac{1}{2}$}	2 MPa	-20 MPa m ^{$-\frac{1}{2}$}	(512.5; 200) pixels

Table 2: Williams' coefficients defining the analytical displacement fields

the measured displacement field. As explained by [19] and [35], a lower radius R_{min} and an upper radius R_{max} must be chosen to define the projection zone. The lower radius is defined to limit the influence of non-linear phenomena near the crack tip and the three-dimensional effects [35]. The upper radius R_{max} is defined to delimit the projection zone.

4. Metrological assessment of the method

Metrological aspects were analyzed to determine the influence of the definition of the projection zone on the estimated values of K_I , T , B and on the crack tip position (noted a) taking into account any potential experimental biases. Considering that the specimen was meticulously machined and adjusted, the impact of potential slight out-of plane motions during loading on measurement biases has been considered as negligible for our purpose. Using equation 3 and some reference parameters (see 2), a true experimental image of a speckle pattern was synthetically deformed using an in-house code. Table 2 shows the values of K_I^{ref} , T^{ref} , B^{ref} and a^{ref} used to generate the analytical displacement. These values were chosen in agreement with Tapered Double Cantilever Beam (TDCB) reference data found in the literature [1, 10, 36] for the material under consideration. Figures 3a and 3b show the displacement fields used to deform the images. U_x and U_y are displacement field components along the x and y directions respectively.

The image was registered using a structured mesh of quadrangular 5 pixels

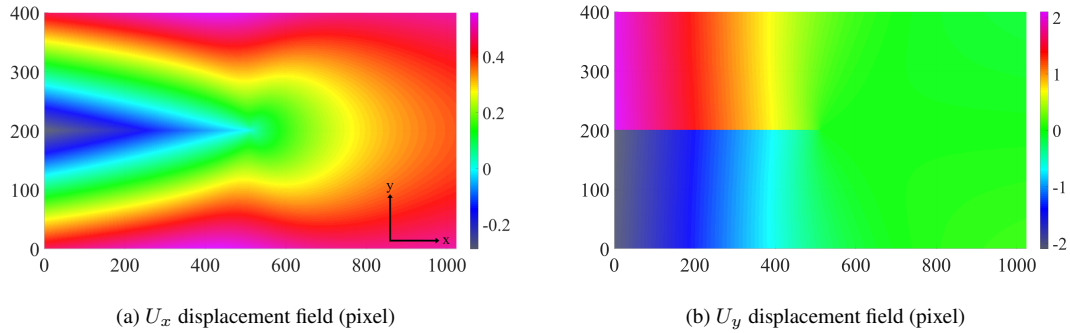


Figure 3: Analytical displacement field (pixel)

	DIC
Image resolution (pixel)	1024 × 400
Type	tiff 8 bits
Pixel size	68 μm
Mesh type	Structured quadrangular
Shape functions	bilinear
Element size	5 pixels
Tikhonov regularization	3 elements

Table 3: DIC parameters

elements using bilinear shape functions. Tikhonov regularization with a cut-off wavelength of 3 elements was considered to filter out spatial noise [37] (see Table 3). The displacement fields obtained with DIC are shown in Figure 4. The latter naturally contains biases from the low-pass filtering of the DIC mesh, DIC convergence, DIC regularization, DIC interpolation and realistic speckle pattern distribution.

DIC displacement fields were projected onto the Williams' series using a least

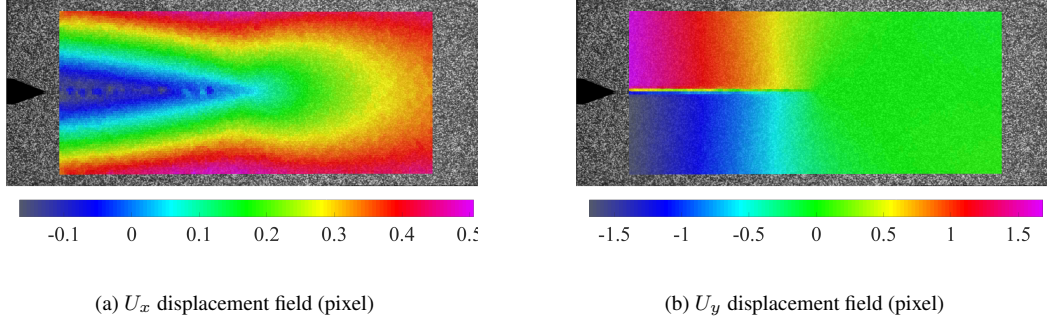


Figure 4: Displacement fields from DIC (quadrangle mesh)

squares approach to identify the different terms K_I , T , B and a . Several projection zones, defined by R_{min} and R_{max} , ranging from 0.05 mm to 1 mm and From 2 mm to 13 mm respectively, were considered to evaluate the influence of these parameters. The projection zone is illustrated in Figure 5. The projection zone on the picture is around the crack tip (defined at the center of the image based on the considered analytical displacement fields see Figure 3b). Elements nearer than R_{min} to the crack are not taken into account. Considering the chosen DIC parameters, for R_{min} lower than 0.4 mm there is no exclusion zone at the crack tip. The maximum value for R_{max} is limited by the image size. The number of data points depends on the values of R_{min} and R_{max} . For example, 1402 nodes were considered with $R_{min} = 1$ mm and $R_{max} = 7$ mm.

The absolute error between target values (see Table 2), noted ref , and the value obtained using DIC, noted o , for K_I , T , B and a was evaluated using the following equations for all projection zones.

$$\epsilon_{K_I} = |K_I^{ref} - K_I^o| \quad (10)$$

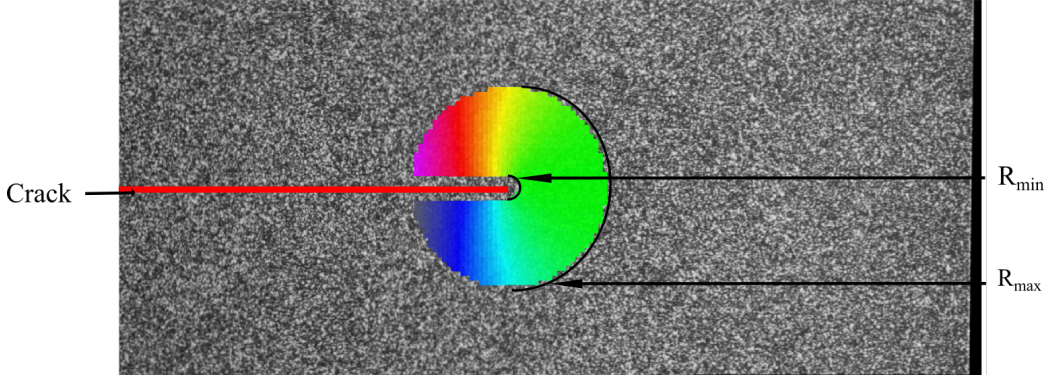


Figure 5: Example of a projection zone for $R_{min} = 1$ mm and $R_{max} = 7$ mm

$$\epsilon_T = |T^{ref} - T^o| \quad (11)$$

$$\epsilon_B = |B^{ref} - B^o| \quad (12)$$

$$\epsilon_a = |a^{ref} - a^o| \quad (13)$$

Firstly, to establish a baseline, the absolute error of each term was evaluated for a noise-free scenario. Figure 6a shows how ϵ_{K_I} varies as a function of R_{min} and R_{max} . For small values of R_{max} , ϵ_{K_I} increases with respect to R_{min} . This is due to the smaller number of nodes (data points) in the projection zone. For high values of R_{max} , ϵ_{K_I} decreases with respect to R_{min} . Then, ϵ_{K_I} decreases with increasing R_{max} . This is due to the greater number of nodes taken into account. To summarize, ϵ_{K_I} is less than $0.03 \text{ MPa m}^{\frac{1}{2}}$ for $R_{max} > 6$ mm independently of R_{min} . Figure 6b shows how ϵ_T varies as a function of R_{min} and R_{max} . Indeed, at first, for low values of $R_{max} < 6$ mm, ϵ_T is higher than 0.5 MPa while for $R_{max} > 6$ mm, ϵ_T decreases with R_{min} . Overall, an increase in R_{max} allows

ϵ_T to decrease. Figure 6c then shows how ϵ_B varies as a function of R_{min} and R_{max} . It is typically greater than $4 \text{ MPa m}^{-\frac{1}{2}}$. ϵ_B is observed to decrease with the increase in R_{max} . The influence of R_{min} is limited. Finally, Figure 6d shows how ϵ_a varies as a function of R_{min} and R_{max} . It is less than 0.4 mm. ϵ_a decreases slightly as R_{min} increases. ϵ_a increases slightly as R_{max} increases. If signed errors are considered (without absolute values), the results are positive for K_I , B and a , *i.e.* the estimates systematically underestimate the actual values. For T , the target value is underestimated when $R_{min} < 0.5 \text{ mm}$ and overestimated when $R_{min} > 0.4 \text{ mm}$.

Camera sensor noise was then added to the images to better mimic experimental conditions. Zero-mean, spatially uncorrelated Gaussian noise is considered. Standard deviation varies with grey level amplitude in agreement with experimental observations (signal-dependent or heteroscedastic noise) from 0.2% to 1.4% of the dynamic spectrum. This noise model was calibrated as follows: noise level was determined from a series of experimental images at rest, by considering standard deviation for each pixel intensity level over time. 11 copies of random noise with a Gaussian distribution and signal-dependent amplitude were created. This noise was added to the reference as well as to the synthetically deformed image. This procedure was run on 5 speckle patterns to take into account pattern-induced biases (see Figure 7). Ultimately, LEFM parameters (K_I , T , B and a with noise for all images denoted K_I^n , T^n , B^n and a^n) were obtained using a similar approach.

For each term, the mean value and standard deviation of K_I^n , T^n , B^n and a^n for the 50 deformed images were considered for the following purpose. The projection zones coincide with those considered in the previous section. The absolute

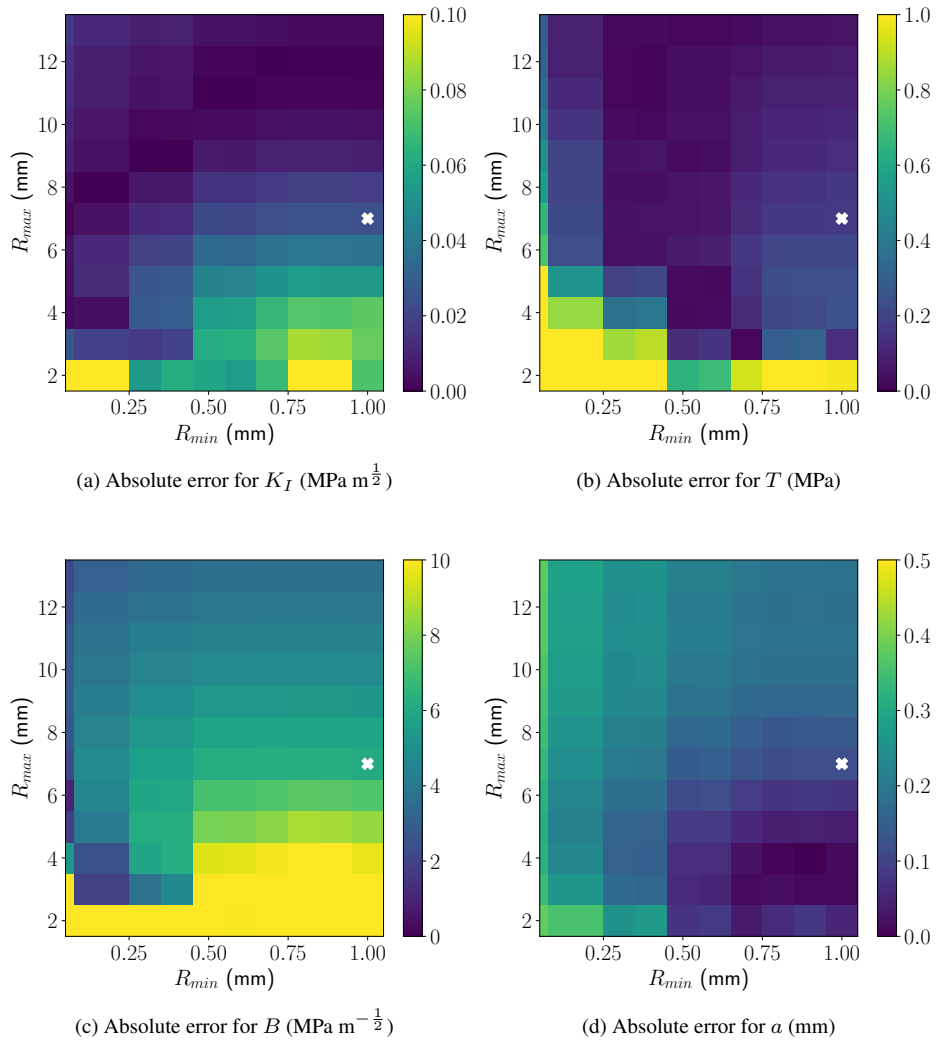


Figure 6: Variation in absolute error for Williams' series terms with R_{min} and R_{max} for the noise-free scenario: (a) variation in ϵ_{K_I} , (b) ϵ_T , (c) ϵ_B and (d) ϵ_a .

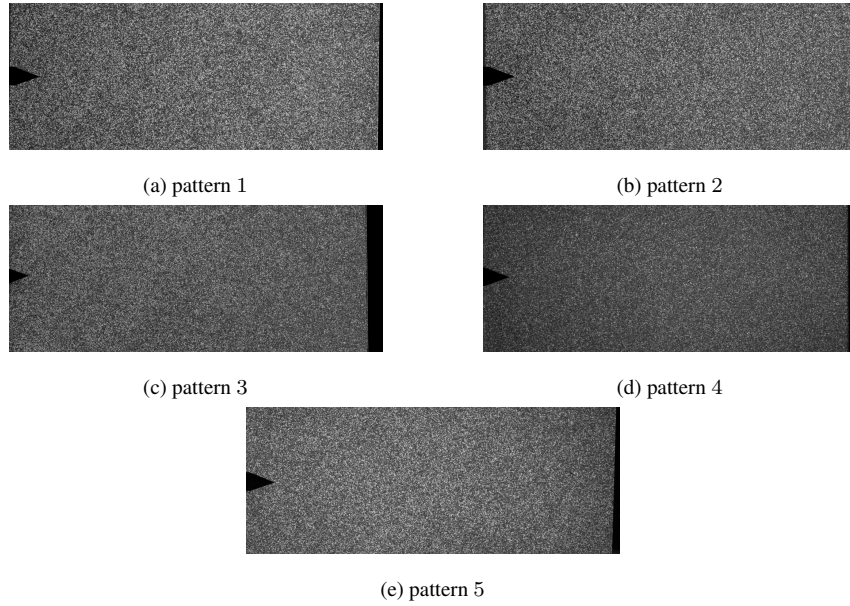


Figure 7: The 5 speckle patterns considered for the metrological assessment

error for each of the Williams' series terms and the crack tip position was determined. The values were found to be slightly higher than in the previous cases. In addition to absolute errors, the standard deviation (noted $\sigma_{K_I^n}$, σ_{T^n} , σ_{B^n} and σ_{a^n}) for each of the Williams' series terms was calculated for all projection zones in order to evaluate measurement uncertainties.

Figures 8a, 8b, 8c and 8d show standard deviation for K_I , T , B and a for all noise scenarios studied (including 5 different speckle patterns). Similar trends can be seen for these three figures: increasing R_{max} with decreasing $\sigma_{K_I^n}$, σ_{T^n} , σ_{B^n} and σ_{a^n} and limited influence for R_{min} . However, the values differ according to the term considered. In Figure 8a, $\sigma_{K_I^n} < 0.01 \text{ MPa m}^{\frac{1}{2}}$ for $R_{max} > 7 \text{ mm}$ independently of R_{min} . In Figure 8b, $\sigma_{T^n} < 0.06 \text{ MPa}$ for $R_{max} > 8 \text{ mm}$ independently of R_{min} . In Figure 8c, $\sigma_{B^n} < 0.6 \text{ MPa m}^{-\frac{1}{2}}$ for $R_{max} > 8 \text{ mm}$ independently of R_{min} . Lastly, in Figure 8d, $\sigma_{a^n} < 50 \text{ }\mu\text{m}$ ($< 1 \text{ pixel}$) for $R_{max} > 5$

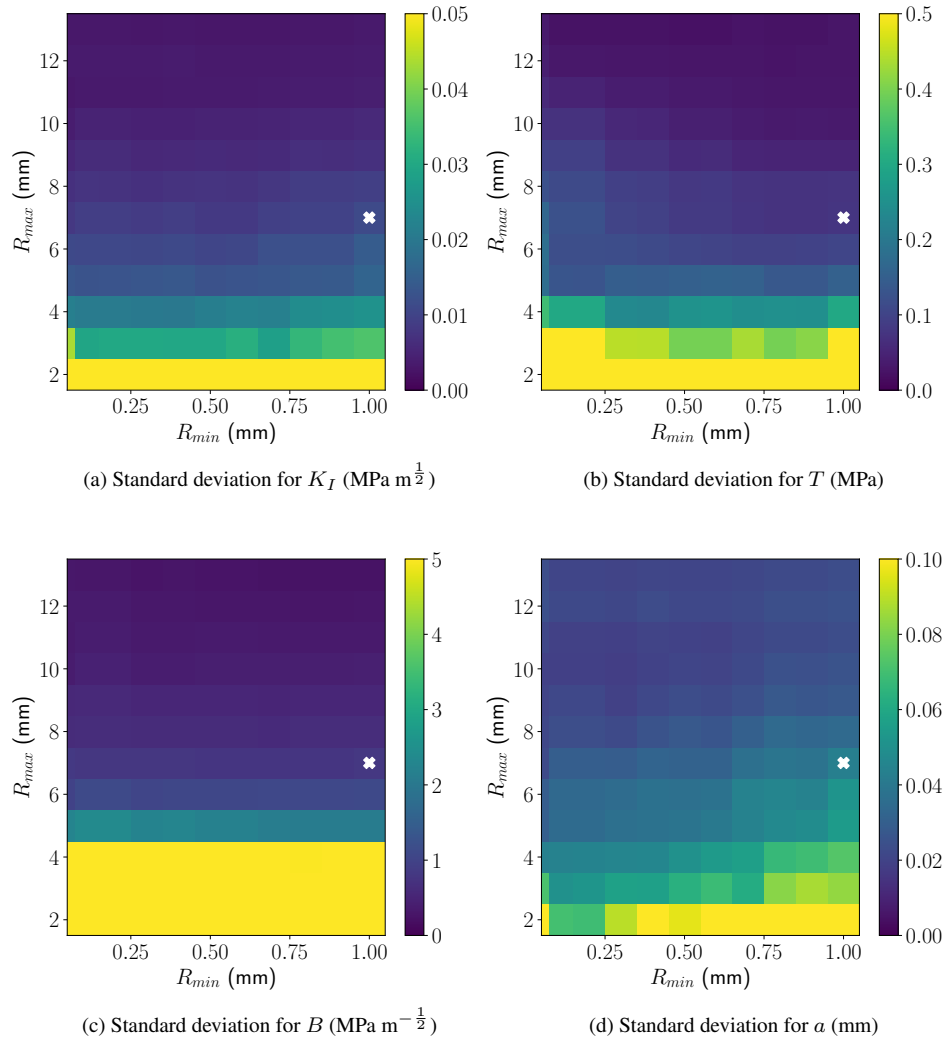


Figure 8: Variation in the standard deviation for the Williams' series terms with respect to R_{min} and R_{max} for the 50 noisy images considered (including 5 different speckle patterns): (a) variation in $\sigma_{K_I^n}$, (b) σ_{T^n} , (c) σ_{B^n} and (d) σ_{a^n} .

	K_I	T	B	a
Absolute error	0.024 MPa m ^½	0.18 MPa	6.9 MPa m ^{-½}	140 μm
Standard deviation	0.011 MPa m ^½	0.077 MPa	0.82 MPa m ^{-½}	43 μm

Table 4: Evaluated mean errors and uncertainties for $R_{max} = 7$ mm and $R_{min} = 1$ mm

mm independently of R_{min} .

The results for the noise-free scenario show that R_{max} can have a significant influence, potentially leading to large standard deviation, especially if $R_{max} < 5$ mm ($\sigma_{T^n} > 5$ MPa and $\sigma_{B^n} > 2$ MPa m^{-½}). A reasonable compromise seems to exist considering $R_{max} > 6$ mm (88 pixels) independently of R_{min} .

To conclude, the impact of the realistic camera noise and the different speckle patterns on identification seems negligible when considering a sufficiently high value of R_{max} . Indeed, absolute variation and standard deviation, for K_I for example, from noise-free to a noisy analysis, remain below 0.03 MPa m^½ and 0.01 MPa m^½ respectively for $R_{max} > 6$, highlighting the robustness of the proposed method. Considering Figure 8, $R_{min} = 1$ mm and $R_{max} = 7$ mm will be used in the following experimental application. Absolute error and standard deviation data for this projection zone are summarized in Table 4. Figure 19 summarizes the different stages of the metrological assessment of the method. Absolute error for a indicates that the evaluation of the crack tip position is reliable to within 140 μm with uncertainty of around 43 μm. This value shows that the crack tip position is reliable for long crack propagation, unlike short crack propagation, where the crack propagation rate can be too slow compared to uncertainty.

5. Experimental set-up

An experimental investigation was carried out using the methodology described in Section 4, on an epoxy resin specimen with two geometries known for inducing different levels of far-field stress. The Hexply®M21 epoxy resin considered was reinforced with thermoplastic nodules to improve its material properties as K_{IC} , creating a non-homogeneous material (as shown in Figure 9). According to the literature [1, 36], the elastic properties of the epoxy resin are $E = 3.1$ GPa and $\nu = 0.35$.

Two specimen geometries (defined in section 8 of the appendix and in Figures 10a and 10b) will be studied in the sequel: a TDCB type geometry known to lead to stable crack propagation [17, 38], and a triangular geometry to induce a different stress field [39], especially a higher magnitude B . A specific protocol was developed to pre-crack all specimens with high repeatability levels. Millimetric pre-cracks were initiated using a cutter blade fixed to the upper holder of an electromechanical tensile test machine, with the specimen secured to the lower holder, by systematically punching the blade into the specimen at a speed of 3.3×10^{-6} m.s⁻¹.

Regarding the fracture experiments, a servo-hydraulic testing device was used at a constant crosshead speed of 10^{-4} m.s⁻¹. The specimen was mounted using adjusted pins (see Figure 11). The load was measured using a 60 kN piezoelectric load cell while the slider displacement was monitored using an optical displacement sensor. Finally, images of the deforming specimen were captured by a high-speed camera. The high-speed camera was used to better record the unwanted stick-slip phenomena systematically arising during tests (see figure 14 and discussion for more details). A uniform black background layer and a white

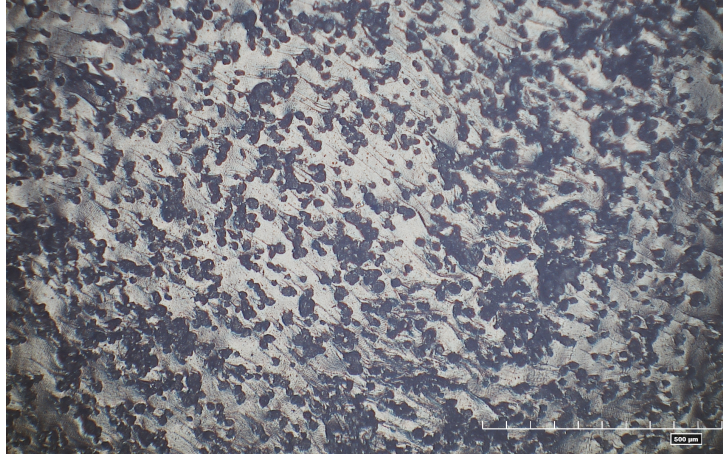
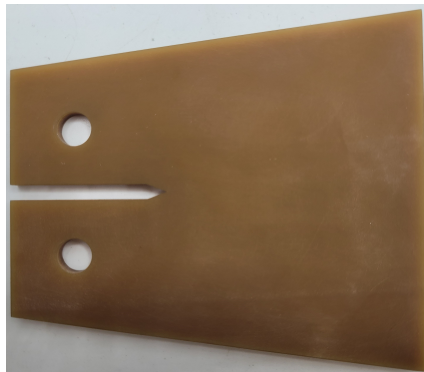
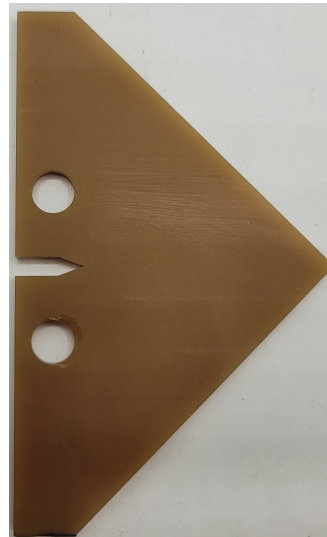


Figure 9: Picture of the thermoplastic nodules included in the Hexply®M21 epoxy resin (500 μm on the scale)



(a)



(b)

Figure 10: Sample geometries considered in this study : (a) TDCB specimen, and (b) triangular specimen

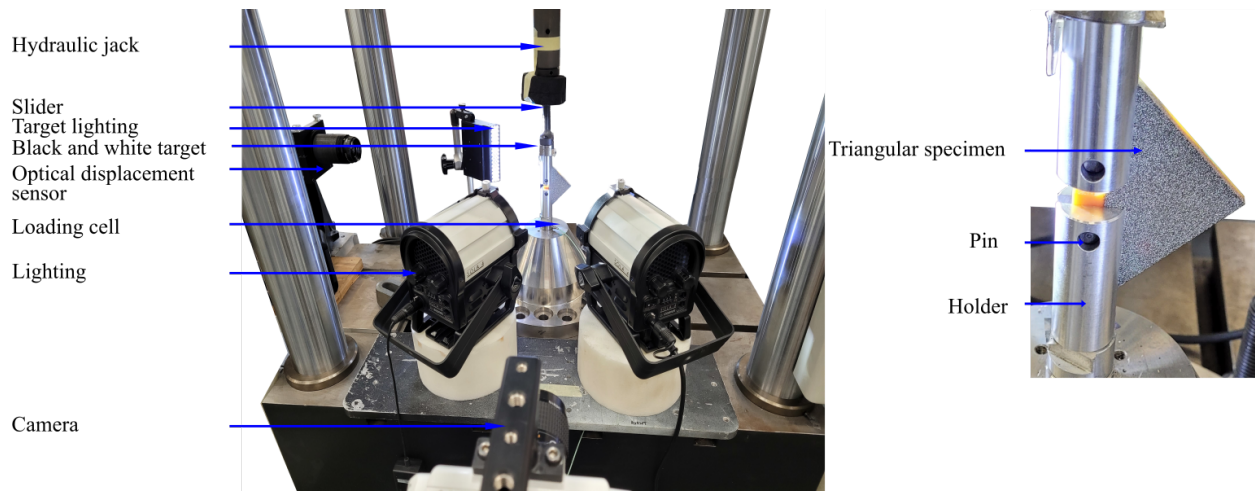


Figure 11: Experimental set-up

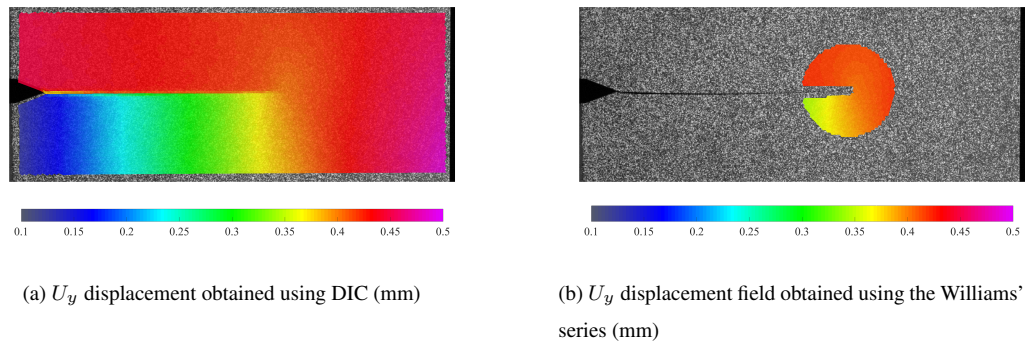


Figure 12: Illustration of the displacement field obtained using DIC and its projection zone onto the Williams' series [31]

Imaging parameters	TDCB specimen	Triangular specimen
Camera	Phantom v2640	
Image resolution (pixel)	1024 × 400	768 × 304
Dynamic range, image	8 bits	
Frame rate	1000 Hz	2000 Hz
Lens	Focal 105 mm Macro Nikkor	
Aperture	f/8	
Field of view	69.6 mm × 27.2 mm	52.2 mm × 20.7 mm
Pixel size	68 μm	
Stand-off distance	70 <i>cm</i>	
Patterning technique	black and white paint	

Table 5: Imaging and camera parameters

speckle-like pattern were sprayed on the specimen surface for the purpose of DIC. The field of view captured all crack propagation during the experiments. Imaging and camera parameters are summarized in Table 5. The image size is 1024 × 400 pixels for TDCB specimens and 768 × 304 pixels for triangular specimens (which are smaller). With these sizes, the frame rate can be increased for triangular specimen experiments while keeping the same physical pixel size. The pixel size considered was equal to 68 μm for all tests. Figures 12a and 12b give an example of the U_y displacement field and its projection onto the Williams' series respectively.

DIC software	Ufreckles
Shape functions	Linear unstructured triangular elements
Element size	5 pixels
Regularization	U: Tikhonov regularization over 3 elements
R_{min} of the projection zone	1 mm
R_{max} of the projection zone	7 mm

Table 6: DIC parameters

6. Results and Discussion

Figure 13a and 13b show post-mortem pictures of the fractured specimens. The crack path for the TDCB specimen remains perfectly straight while, with the triangular specimen, the crack deviates when approaching the edges of the specimen. A similar response can be observed in other studies [2, 39]. The methodology described earlier was used to determine K_I , T and B for each specimen. K_I , T and B are shown in Figures 14, 16a and 16b.

Figure 14 shows variation in K_I with respect to the normalized crack propagation distance. The latter is defined by the ratio $\frac{a_x}{w}$, *i.e.* the ratio between the distance along the horizontal axis from the crack tip to the center of the pins and the distance along the horizontal axis between the center of the pins and the left end of the specimen. Similar normalization can be found in [5]. More details are provided in Table 7 and in Figure 22 of the appendix section.

Two principal trends can be observed: intermittent behaviour is clearly apparent in Figure 14. Indeed, for both specimen geometries, crack propagation is periodically interrupted by dynamic unstable jumps (of about 7 mm for the TDCB specimen and 2.5 mm for the triangular specimen). Dynamic jumps are

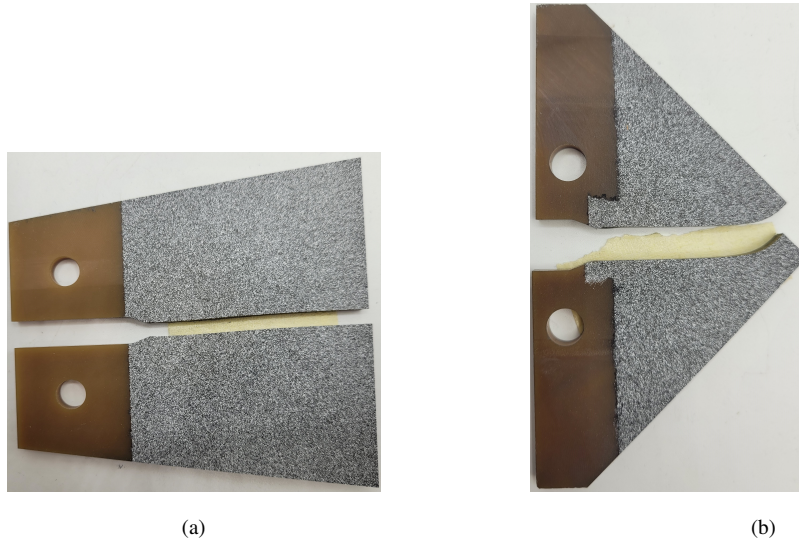


Figure 13: Post-mortem picture of the specimen : **a)** TDCB specimen, and **b)** triangular specimen.

not visible when the crack propagates at about 100 m.s^{-1} due to the temporal resolution used [40]. Such a phenomenon has already been observed and discussed *e.g.* for PMMA, by some authors [41–44]. It is usually named stick-slip in reference to adhesive behaviour or intermittent/avalanche propagation. However, this phenomenon is still poorly understood and seems to relate to some sort of thermo-viscoelastic effect [42] inducing a domain of unwanted crack velocities [40]. Interestingly, while PMMA and the Hexply®M21 epoxy resin have almost similar elastic properties ($E = 3.5 \text{ GPa}$, $\nu = 0.3$), contrary to PMMA, no loading condition eliminating such unstable behaviour has been identified ; neither extremely low loading rates (down to 0.01 mm.min^{-1} - not shown here), nor low temperatures (down to -3° C - even if the amplitude of the instabilities is decreased - not shown here), are compatible with non-intermittent, but fully dynamic propagating cracks, only high-rate loading (*i.e.* beyond the stable domain - not shown here) is compatible. The fact that triangular geometry mitigates the phenomenon implies

that the local stress state in the vicinity of the crack tip (modified by structural effects) may play a significant role, but a thorough investigation of stick-slip phenomenon is out of the scope of this study.

Putting on a side value at initiation (*i.e.* near the laser cut notch - see $\frac{a_t}{w} \approx 0.1$) and zooming in on quasi-static stable phases, K_I systematically increases from around 0.8 to 1.2 MPa m^{1/2} (see Figure 14) when it stabilizes. K_I then systematically jumps back to a lower value during the dynamic propagation phase. Such a trend for K_I , within stable propagation phases, may be associated with a reoccurring initiation process before reaching Griffith regime [15, 45, 46] and a new dynamic phase.

When exclusively considering quasi-static propagation phases in Figure 14 (*i.e.* when the crack propagates at a slow cracking rate), only certain values of K_I are taken into account before each dynamic propagation phase (see the gray corridor in Figure 14). Standard deviation, $\sigma_{K_I^n}$, obtained in metrological section 4 (see Table 4) was chosen as a metric to select the points in a "stable" propagation regime prior to the start of dynamic instability. From the unstable phase, the set of data points considered expanded until reaching a standard deviation of two $\sigma_{K_I^n}$ (see 4). The reduced set of K_I data is presented with respect to the normalized crack propagation distance in Figure 15. For the TDCB specimen, the values of K_I for each quasi-static propagation phase and for each experiment are very similar with a mean $K_I = 1.06$ MPa m^{1/2}. A similar trend is apparent for triangular specimens (mean value of 1.03 MPa m^{1/2}) although a slight decrease appears when approaching the right edge of the specimen ($\frac{a_t}{w} > 0.7$). Even if stress intensity

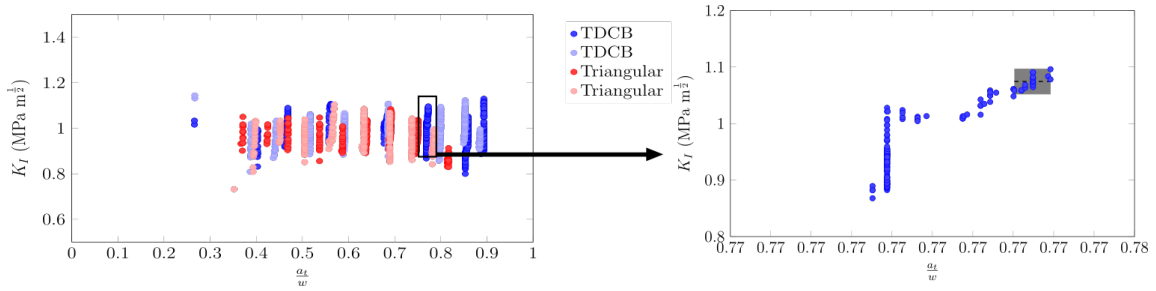


Figure 14: K_I as a function of the normalized crack propagation distance

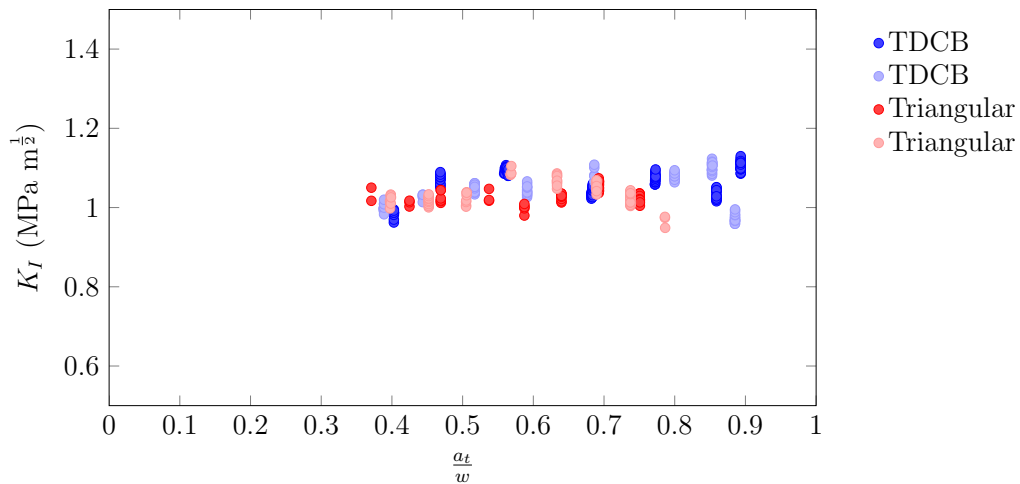


Figure 15: K_I as a function of the normalized crack propagation distance

factors are globally similar, variations exceed estimated metrological uncertainties from the start ($\frac{a_t}{w} \approx 0.35$) to the end of propagation ($\frac{a_t}{w} > 0.75$).

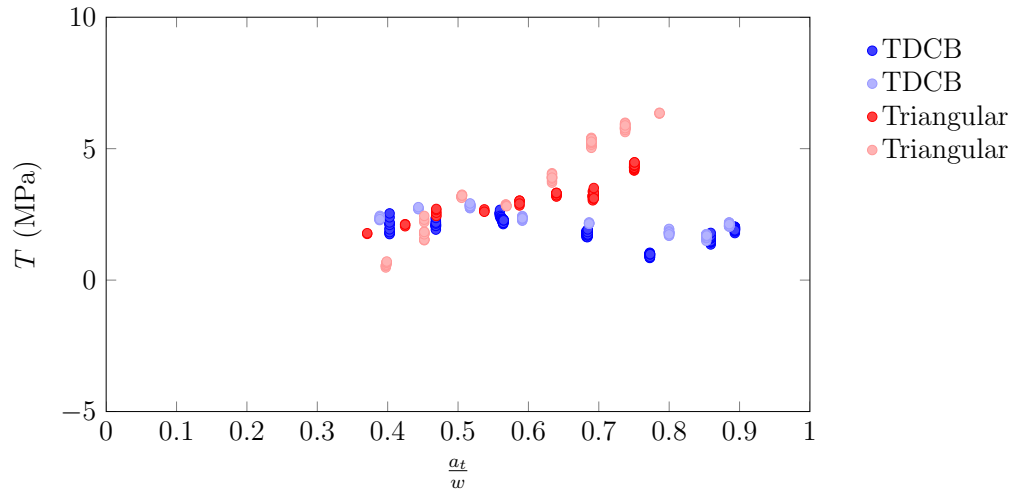
For a more in-depth analysis of such variations, let us now discuss how T and B vary with respect to the propagation distance for the two geometries considered. The same data set reduced to a stable propagation regime is considered. Figure 16a shows variation in T with respect to the normalized crack propagation distance. Two global trends are apparent. For TDCB specimens, T varies

between 0.85 and 3.5 MPa with a mean value of 2 MPa. For triangular specimens, T increases during crack propagation. It is lower at the start of crack propagation, when T is negative, and progressively increases, reaching 5 MPa by the end of propagation.

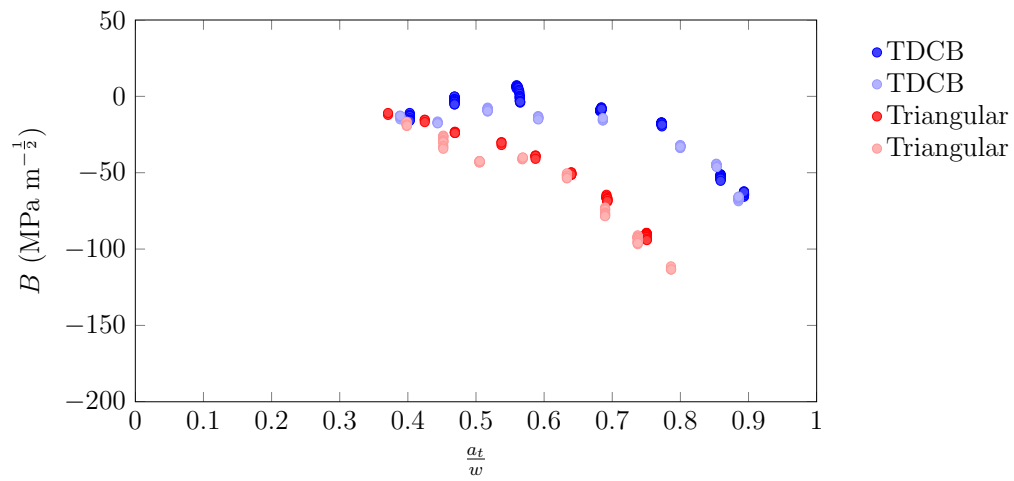
With TDCB specimens, according to the literature, this specimen allows for stable crack propagation [17, 38]. T values are positive but remain low (compared to the strength of the material) which ensures a stable crack propagation direction. With triangular specimens, T is observed to increase, causing the crack to rotate at the end of propagation, as is apparent in our scenario (see Figure 13). In the literature, several authors have shown that crack direction is impacted by T [2, 4, 7, 8, 47]. In particular Meliani *et al.* explained that a negative T stabilizes the crack path whereas a positive T can lead to crack bifurcations, which indeed occurs with the triangular specimens [47].

Figure 16b shows how B varies with respect to normalized crack propagation distance. As for T , two global trends can be observed for B depending on the specimen geometry. For the TDCB specimens, the values remain close to $-9 \text{ MPa } m^{-\frac{1}{2}}$ up to a normalized crack propagation distance of 0.6. At the end of crack propagation, B decreases to $-70 \text{ MPa } m^{-\frac{1}{2}}$. For the triangular specimens, B decreases more significantly and abruptly. B starts at $-10 \text{ MPa } m^{-\frac{1}{2}}$ and drops down to $-115 \text{ MPa } m^{-\frac{1}{2}}$. In contrast to the TDCB specimen, B decreases from the very start of propagation. The geometry-dependent stress field is clearly apparent for the T and B parameters.

Let us now discuss variation in K_{IC} with respect to T and B to better understand the link between far-field stress and actual K_{IC} . Just like in the aforemen-

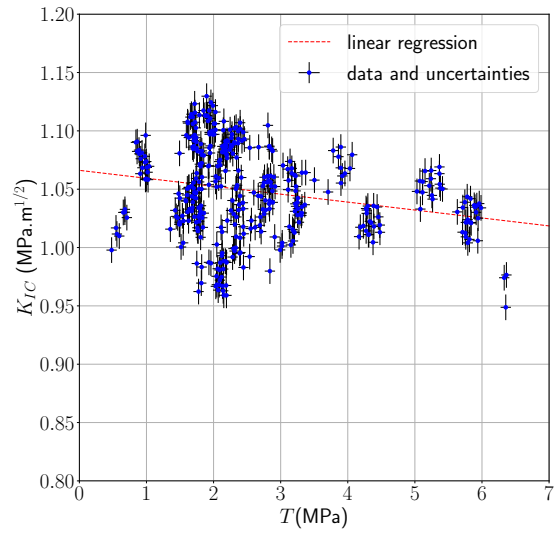


(a)

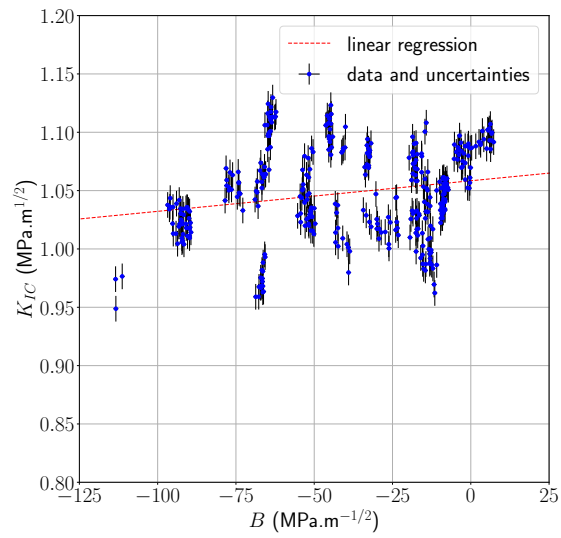


(b)

Figure 16: Crack tip parameters evolution with respect to the normalized crack propagation : **(a)** T and **(b)** B



(a) $K_{IC} = -6.80 \pm 0.8 \times 10^{-3} T + 1.07 \pm 0.00$; $\chi_r^2 = 11.29$



(b) $K_{IC} = 0.26 \pm 0.04 \times 10^{-3} B + 1.06 \pm 0.00$; $\chi_r^2 = 11.40$

Figure 17: Crack tip parameters. (a) K_{IC} with respect to T and (b) K_{IC} with respect to B

tioned literature, we started with a mono-parametric approach. Figures 17a and 17b show the data. Unlike previous authors, who only focused on one type of data per experiment, the proposed method is compatible with a significant amount of data per experiment. In both cases, linear regression and experimental uncertainties (see red line and error bars respectively) were added in order to discuss the relevance (compared to estimated metrological uncertainties) of the variation in K_{IC} with respect to T and B . Uncertainty zones cover \pm estimated metrological standard deviation for K_I , T and B (0.011 MPa m $^{\frac{1}{2}}$, 0.077 MPa, 0.82 MPa m $^{-\frac{1}{2}}$ - see Table 4).

Regarding the relationship K_{IC} vs T (see Figure 17a) the linear regression highlights a slight decrease in K_{IC} with respect to T . The linear regression equation and its reduced chi-squared value, χ_r^2 (*i.e.* the ratio between the deviation from the model and estimated measurement uncertainties), have also been added to the figure. The identified slope is shallow, about $-6.80^{\pm 0.8} \times 10^{-3} \text{ m}^{\frac{1}{2}}$ with variation in K_{IC} , over the range studied, reaching only 0.05 MPa m $^{\frac{1}{2}}$. It is nevertheless about 5 times the estimated metrological uncertainty and the 95% confidence interval for the slope is around 12 %. $\chi_r^2 = 11.29 \gg 1$ indicating that the actual dispersal around the linear regression line is much greater than estimated metrological uncertainty, hence (1) either a linear model is an oversimplification or (2) the uncertainties were underestimated. Regarding the last point some elements potential out-of-plane motions and or Poisson's effect, light variation) and the metrological analysis was carried out using a linear analytical solution for the displacement field whereas, in practice, behaviour may be non-linear near and around the crack tip. Secondly, the solution proposed for filtering out the im-

pact of reoccurring stick-slip phenomena is not systematically fully efficient in terms of eliminating the consequences of dynamic instability. Indeed, although the K_{IC} values shown only encompass the stable toughness domain before reoccurring dynamic instabilities, it is not yet clear how much the values are affected by this phenomenon. Instability may be the most probable source of the apparent scattering, however it could not have caused the observed slope. In Figure 17b, B varies from -120 to $10 \text{ MPa m}^{-\frac{1}{2}}$. Here, a slight increase in K_{IC} can be observed with respect to B . The slope is $0.26^{\pm 0.04} \times 10^{-3} \text{ m}$ with about $0.06 \text{ MPa m}^{\frac{1}{2}}$ variation in K_{IC} . Again, these values are small but, as is the case for T , remain about 6 times higher than estimated metrological uncertainty. The 95% confidence interval for the slope is around 15%, which is worse than previously. As for T , $\chi_r^2 = 11.40 \gg 1$ leading to similar conclusions.

In the light of figures 17a and 17b, we can tenuously conclude that T and B impact K_{IC} in Hexply®M21 epoxy resin over the range investigated. However, from a statistical point-of-view, the exact nature of the relationship cannot be established. Besides, T and B vary simultaneously for both experiments. If we uncouple their contributions, by analyzing K_{IC} in T vs B space, both potentially appear as crack tip loading parameters, which is more relevant. This effect is shown in Figure 18. A bi-linear regression is applied. The equation has been added to the figure caption. On this basis, the relationship between K_{IC} and T or B can be determined separately. While global trends are similar, *i.e.* a slight negative, respectively positive slope of K_{IC} as a function of T , respectively B , identified values are smaller. Especially, the linear dependency with respect to B is divided by 2. These results show that the bi-linear relationship confirms the

previous mono-parametric approach to determine K_{IC} .

The bi-linear approximation:

$$K_{IC} = -4.84^{\pm 0.6} \times 10^{-3} T + 0.12^{\pm 0.02} \times 10^{-3} B + 1.07^{\pm 0.00} \quad (14)$$

seems nevertheless a more relevant fit of the experimental dataset considering implicit couplings between B and T that a 2D fit can not properly capture. Considering for example SENT configuration presented in Figure 2b where $B \approx 300 \text{ MPa m}^{-\frac{1}{2}}$, it would induce more than 4 % variation in K_{IC} from its nominal value. The latter can be approached when B and T are null. Referring to Figure 17a, 17b or 18, the y-intercept remains highly consistent, $K_{IC}^n \approx 1.07 \text{ MPa m}^{\frac{1}{2}}$. As for previous linear regressions for T and B , $\chi_r^2 = 11.26 \gg 1$ leading to similar conclusions regarding the exact nature of the dependence.

Outstanding issue. The following model should nevertheless be interpreted with caution. Indeed, as it has been previously explained, a choice has been made when defining the *relevant* K_I values for the determination of K_{IC} . So far, stable and pre-dynamic instability values have been considered as relevant. However, the literature does not agree on the propagation phase to consider, for determining K_{IC} , in presence of stick-slip instabilities. Some authors have discussed both cases, using pre- (initiation) and post-dynamic (arrest values) instability values for determining K_{IC} or G_{IC} [48–50]. In composite materials, Daghia *et al.* have highlighted that the values of G_{IC} obtained from each load peaks are greater than the values obtained by considering the dissipated energy during the load drops

[51]. Lastly, Bandyopadhyay [52] has explained that the value of K_I before dynamic instability overestimates K_{IC} due to the plastic deformation at the crack tip leading to crack tip blunting. According to the author, the value of K_I for crack arrest is closer to the value of K_I for continuous crack propagation. Without a clear answer regarding the choice of pre- or post-dynamic instability values for K_{IC} determination, both alternative could eventually be considered. In that context, Equation 15 presents the bi-linear $K_{IC} = f(T, B)$ relationship obtained when considering post-dynamic crack propagation phases. In practice, the considered set of data points starts from the value just after the dynamic crack propagation and extends until it reaches a standard deviation of twice $\sigma_{K_I^n}$ (see Table 4).

$$K_{IC} = -1.9^{\pm 0.6} \times 10^{-3} T + 0.4^{\pm 0.03} \times 10^{-3} B + 0.93^{\pm 0.00} \quad (15)$$

K_{IC} vs T slope is lower than the one obtained previously in equation 14. In contrast, K_{IC} vs B slope is greater from that observed in equation 15. Nevertheless global trends remain consistent. These results show that when considering post-dynamic instability values, the dependencies of K_{IC} to B and T are respectively of greater and lower amplitude than the ones observed when considering pre-instability values. This relation eventually translates a tenuous sensitivity of K_{IC} to B , and no quantifiable sensitivity to T , at least over the studied loading range. Using this previous equation, the nominal value $K_{IC}^n \approx 0.93 \text{ MPa m}^{\frac{1}{2}}$ which is significantly lower than K_{IC}^n got from equation 14. This result is in agreement with the literature which explained that the arrest K_I values are lower than the initiation ones. For this post-dynamic instability regression, $\chi_r^2 = 7.36 \gg 1$ leading to similar conclusions regarding the exact nature of the dependence. Nevertheless, the value is significantly lower than the one obtained considering pre-

instability values, meaning that there is less dispersion when considering post-dynamic instability values.

7. Conclusion

In this paper, full-field imaging techniques were used to shed light on the link between a far-field stress state and K_{IC} in Hexply®M21 epoxy resin as well as, more generically, between specimen geometry and such far-field stress. Literature shows the significant effect of B and T on estimated K_{IC} for quasi-brittle material (especially PMMA) during quasi-static propagation. Our objective was to investigate how full-field measurements (using DIC) coupled with Williams' series expansion could be used as part of a local identification approach to confirm or refute such trends in epoxy resin and potentially better predict the fracture responses of cohesive cracks confined in composite materials. Metrological aspects of the method were initially assessed to investigate the influence of analytical and experimental parameters such as the projection zone, camera sensor noise and speckle pattern variation. In the noise-free scenario, the most impacting parameter of the proposed methodology was found to be R_{max} . If values are too small ($R_{max} < 6 \text{ mm}$), significant identification errors arise for K_I , T , B and crack tip position. The influence of R_{min} is limited, especially for B . Noise and speckle variations induce limited uncertainty ($< 0.01 \text{ MPa m}^{\frac{1}{2}}$) for K_I if R_{max} is kept large enough ($R_{max} > 6 \text{ mm}$). The proposed method was then applied to Hexply®M21 epoxy resin specimens with two different geometries, TDCB and triangle, known to record T and B space reasonably well while being compatible with full-field imaging techniques. No quasi-static, room temperature, solution has

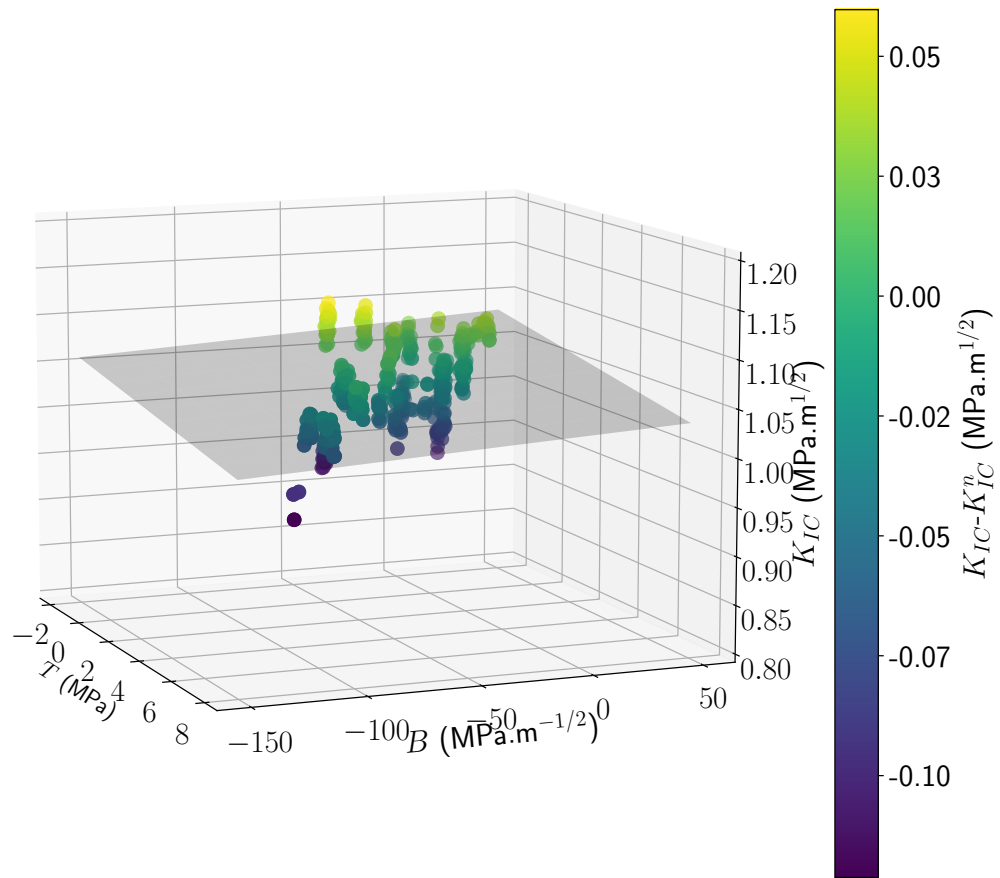


Figure 18: Variation in K_{IC} with respect to T and B . The colour gradient corresponds to the K_{IC} values ; $K_{IC} = -4.84^{\pm 0.6} \times 10^{-3} T + 0.12^{\pm 0.02} \times 10^{-3} B + 1.07^{\pm 0.00}$; $\chi_r^2 = 11.26$

been found to eliminate stick-slip-like behaviour (*i.e.* dynamic instability), unlike PMMA which has similar elastic properties (not presented in this document). The microstructure of the material, made of thermoplastic nodules, may influence the unwanted triggering or initiation of such instability. A solution was ultimately proposed to discard some data, while only retaining the systematic stable toughness domain before reoccurring dynamic instability for analysis. The influence of specimen geometry on T and B was clearly demonstrated with an ultimate B value about 2 times higher (in amplitude) for a triangular specimen than for a TDCB specimen. T remained stable for the TDCB specimen, at about 2 MPa, and B only varied slightly, which increased near the edge of the specimen. Triangular specimens show both a significant increase in T and a significant decrease in B (down to $-115 \text{ MPa}\cdot\text{m}^{-\frac{1}{2}}$). Finally, if we consider a bi-linear regression of K_{IC} in B vs T space, two trends appear: 1) a slight increase in K_{IC} as a function of B as well as 2) a slight decrease of K_{IC} as a function of T at least within the B vs T loading domain studied. The B trend exceeds estimated experimental uncertainties, but remains extremely tenuous and should be confirmed by exploring more values of T and B . However, even if the observed influence of B (possibly T) on K_{IC} for the resin remains minor, it is important to take note that numerical simulations mimicking the confined state of a resin between fibers (not presented in this document) have given B values of around hundreds $\text{MPa}\cdot\text{m}^{-\frac{1}{2}}$, *i.e.* far beyond the B range investigated in the literature (including this work). Considering such a stress state and according to the dependencies observed in this work, K_{IC} would vary between 5 % and 20 % from its nominal value (depending on data kept (pre- or post-dynamic instability) for building the model). If such variations can be confirmed for large B values, using, for example, double cleavage drilled com-

pression (DCDC) or SENT specimen geometries, the development of extended fracture criteria depending on *e.g.* K_I and B (eventually T) may be required. An additional perspective would be to use such a framework to investigate the influence of crack propagation rate on K_{IC} for confined cracks in epoxy resins since the proposed methodology does not require load measurements, which are usually impossible to accurately record at high speeds.

Acknowledgements

We would like to thank Hexcel composite and especially Mr.Fournier-Le-Ray for supplying the material and La Région Pays-de-La Loire for funding this work.

CRedit authorship contribution statement

Bastien Lammens : Conceptualization, Data curation, Investigation, Writing – original draft. **Gérald Portemont** : Conceptualization, Project administration, Resources, Investigation, Supervision, Writing – review & editing. **Julien Berthe** : Conceptualization, Project administration, Resources, Investigation, Supervision, Writing – review & editing. **Rian Seghir** : Conceptualization, Project administration, Investigation, Supervision, Writing – review & editing. **Julien Réthoré** : Conceptualization, Project administration, Investigation, Software, Supervision, Validation, Writing – review & editing.

Declaration of Competing Interest

Conflict of interest :

The authors declare that they have no conflict of interest.

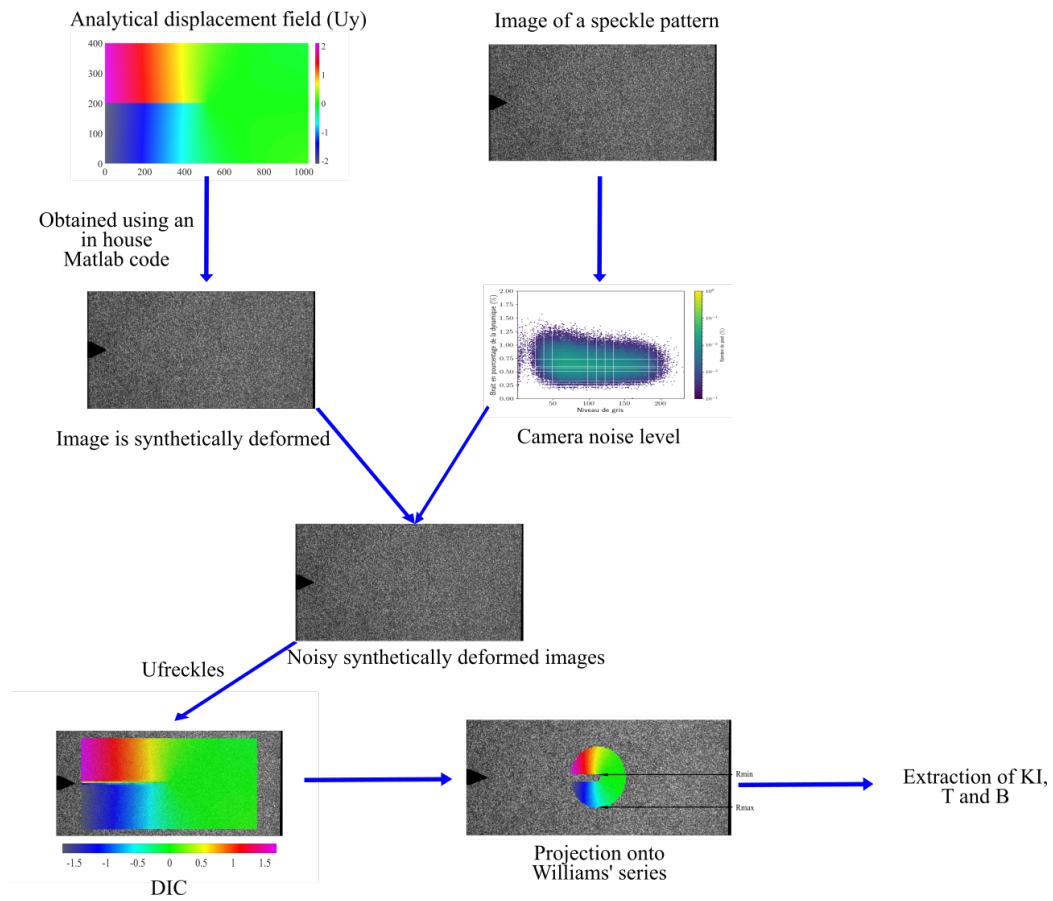


Figure 19: Diagram of metrological assessment stages

8. Appendix

8.1. A

8.2. B

For more information about the different sizes of the specimens considered, diagrams can be found in Figures 20 and 21.

8.3. C

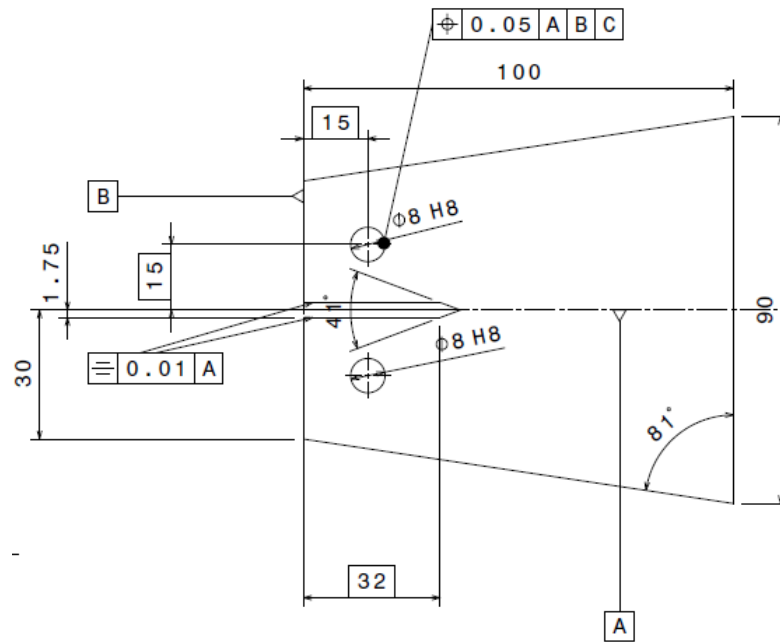


Figure 20: Sketch of the TDCB specimen

Normalized crack length	TDCB specimen	Triangular specimen
a	$[0 : 63.5]$ mm	$[0 : 47.5]$ mm
a_2	$36.5 - 15 = 21.5$ mm	$12.5 - 7 = 5.5$ mm
w	$100 - 15 = 85$ mm	$60 - 7 = 53$ mm
a_t	$a + a_2$	$a + a_2$
N_a	$\frac{a_t}{w}$	$\frac{a_t}{w}$

Table 7: Normalized crack length

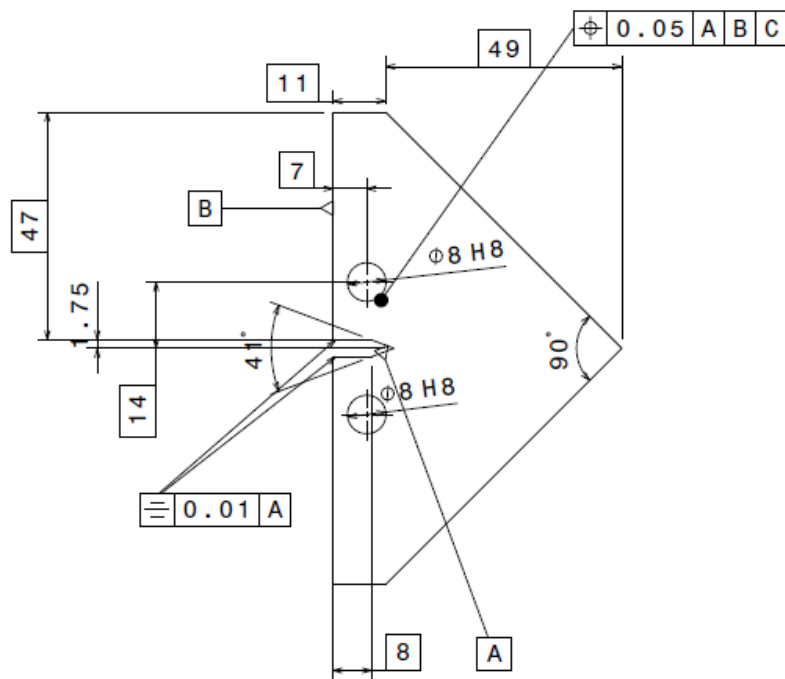


Figure 21: Sketch of the triangular specimen. While not required for analysis, take note notice that the notch radius is less than 0.1 mm

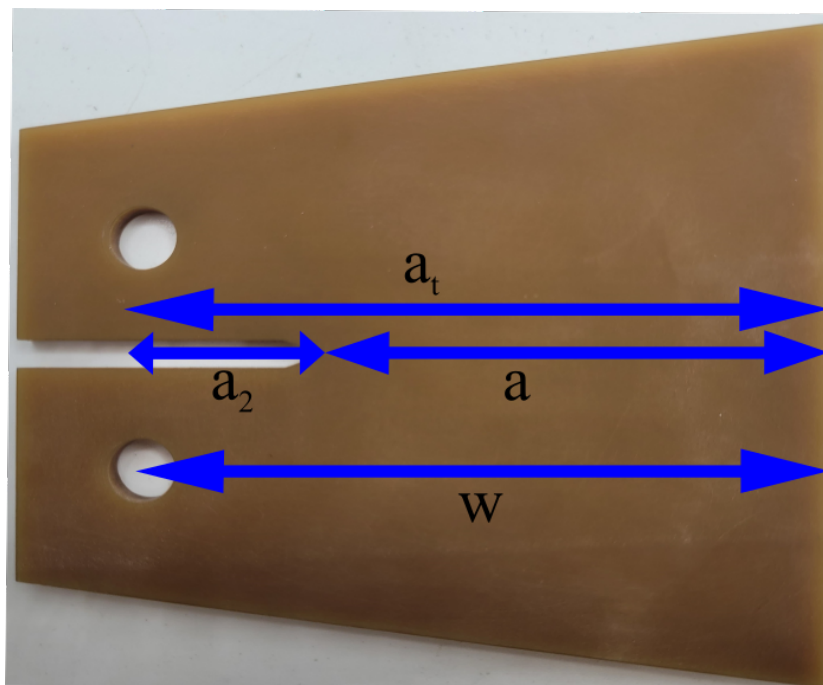


Figure 22: TDCB specimen with the normalized crack length

References

- [1] V. Joudon, Caractérisation expérimentale de l'initiation et de la propagation de fissure dans une résine époxy sous chargement dynamique, Ph.D. thesis, Université de Valenciennes et du Hainaut-Cambresis (2014).
- [2] M. Ayatollahi, M. R. Moghaddam, S. Razavi, F. Berto, Geometry effects on fracture trajectory of pmma samples under pure mode-I loading, *Engineering Fracture Mechanics* 163 (2016) 449–461.
- [3] M. Ayatollahi, M. Pavier, D. Smith, Mode I cracks subjected to large t-stresses, *International Journal of Fracture* 117 (2002) 159–174.
- [4] O. Bouledroua, M. H. Meliani, G. Pluinage, A review of t-stress calculation methods in fracture mechanics computation, *Nature & Technology* (15) (2016) 20.
- [5] B. Cotterell, J. Rice, Slightly curved or kinked cracks, *International journal of fracture* 16 (1980) 155–169.
- [6] B. Cotterell, Notes on the paths and stability of cracks, *International Journal of Fracture Mechanics* 2 (1966) 526–533.
- [7] S. M. J. Razavi, M. Ayatollahi, F. Berto, A synthesis of geometry effect on brittle fracture, *Engineering Fracture Mechanics* 187 (2018) 94–102.
- [8] M. Gupta, R. Alderliesten, R. Benedictus, A review of t-stress and its effects in fracture mechanics, *Engineering Fracture Mechanics* 134 (2015) 218–241.

- [9] B. Kumar, S. Chitsiriphanit, C. Sun, Significance of k-dominance zone size and nonsingular stress field in brittle fracture, *Engineering Fracture Mechanics* 78 (9) (2011) 2042–2051.
- [10] Y. Chao, S. Liu, B. Broviak, Brittle fracture: variation of fracture toughness with constraint and crack curving under mode I conditions, *Experimental Mechanics* 41 (2001) 232–241.
- [11] Y.-J. Chao, X. H. Zhang, Constraint effect in brittle fracture, *ASTM special technical publication* 1296 (1997) 41–60.
- [12] S. Morel, G. Mourot, J. Schmittbuhl, Influence of the specimen geometry on r-curve behavior and roughening of fracture surfaces, *International Journal of Fracture* 121 (2003) 23–42.
- [13] R. W. Steinbrech, A. Reichl, W. Schaarwächter, R-curve behavior of long cracks in alumina, *Journal of the American Ceramic Society* 73 (7) (1990) 2009–2015.
- [14] T. Fett, D. Munz, R. Geraghty, K. White, Influence of specimen geometry and relative crack size on the r-curve, *Engineering Fracture Mechanics* 66 (4) (2000) 375–386.
- [15] M. L. Williams, On the stress distribution at the base of a stationary crack, *Journal of Applied Mechanics* (1957).
- [16] A. Ghasemi-Ghalebahman, A. A. Aghdam, S. Pirmohammad, M. H. Nikaki, Experimental investigation of fracture toughness of nanoclay reinforced polymer concrete composite: Effect of specimen size and crack angle, *Theoretical and Applied Fracture Mechanics* 117 (2022) 103210.

- [17] T. M. Grabois, J. Neggers, L. Ponson, F. Hild, R. D. Toledo Filho, On the validation of integrated dic with tapered double cantilever beam tests, *Engineering Fracture Mechanics* 191 (2018) 311–323.
- [18] C. Roux-Langlois, A. Gravouil, M.-C. Baietto, J. Réthoré, F. Mathieu, F. Hild, S. Roux, Dic identification and x-fem simulation of fatigue crack growth based on the williams' series, *International Journal of Solids and Structures* 53 (2015) 38–47.
- [19] J. Réthoré, Automatic crack tip detection and stress intensity factors estimation of curved cracks from digital images, *International Journal for Numerical Methods in Engineering* 103 (7) (2015) 516–534.
- [20] R. Harilal, C. Vyasrayani, M. Ramji, A linear least squares approach for evaluation of crack tip stress field parameters using dic, *Optics and Lasers in Engineering* 75 (2015) 95–102.
- [21] J. R. Yates, M. Zanganeh, Y. H. Tai, Quantifying crack tip displacement fields with DIC, *Engineering Fracture Mechanics* 77 (11) (2010) 2063–2076.
- [22] M. R. Ayatollahi, M. Moazzami, Digital image correlation method for calculating coefficients of williams expansion in compact tension specimen, *Optics and Lasers in Engineering* 90 (2017) 26–33.
- [23] M. A. Sutton, W. Wolters, W. Peters, W. Ranson, S. McNeill, Determination of displacements using an improved digital correlation method, *Image and vision computing* 1 (3) (1983) 133–139.
- [24] M. A. Sutton, J. J. Orteu, H. Schreier, Image correlation for shape, motion

and deformation measurements: basic concepts, theory and applications, Springer Science & Business Media, 2009.

- [25] G. Besnard, F. Hild, S. Roux, “finite-element” displacement fields analysis from digital images: application to portevin–le châtelier bands, *Experimental mechanics* 46 (2006) 789–803.
- [26] J. Réthoré, F. Hild, S. Roux, Extended digital image correlation with crack shape optimization, *International journal for numerical methods in engineering* 73 (2) (2008) 248–272.
- [27] M. Ayatollahi, M. Nejati, An over-deterministic method for calculation of coefficients of crack tip asymptotic field from finite element analysis, *Fatigue & Fracture of Engineering Materials & Structures* 34 (3) (2011) 159–176.
- [28] M. R. Ayatollahi, M. Nejati, S. Ghoulif, The finite element over-deterministic method to calculate the coefficients of crack tip asymptotic fields in anisotropic planes, *Engineering Fracture Mechanics* 231 (2020) 106982.
- [29] E. Eid, Towards a multi-scale analysis of dynamic failure in architected materials, Ph.D. thesis, Ecole Centrale de Nantes (2022).
- [30] Standard test method for poisson’s ratio at room temperatures, ASTM E132-92, *Annual Book of ASTM Standards*, 03.01 (1993) 323–325.
- [31] J. Réthoré, UFreckles, language: eng (Oct. 2018). doi:10.5281/zenodo.1433776.
- [32] R. Hamam, F. Hild, S. Roux, Stress intensity factor gauging by digital image correlation: Application in cyclic fatigue, *Strain* 43 (3) (2007) 181–192.

- [33] J. Réthoré, R. Estevez, Identification of a cohesive zone model from digital images at the micron-scale, *Journal of the Mechanics and Physics of Solids* 61 (6) (2013) 1407–1420.
- [34] S. Roux, J. Réthoré, F. Hild, Digital image correlation and fracture: an advanced technique for estimating stress intensity factors of 2d and 3d cracks, *Journal of Physics D: Applied Physics* 42 (21) (2009) 214004.
- [35] G. P. Mogadpalli, V. Parameswaran, Determination of stress intensity factor for cracks in orthotropic composite materials using digital image correlation, *Strain* 44 (6) (2008) 446–452.
- [36] V. Joudon, G. Portemont, F. Lauro, B. Bennani, Experimental procedure to characterize the mode I dynamic fracture toughness of advanced epoxy resins, *Engineering Fracture Mechanics* 126 (2014) 166–177.
- [37] T. Poggio, H. Voorhees, A. Yuille, A regularized solution to edge detection, *Journal of Complexity* 4 (2) (1988) 106–123.
- [38] IM.Daniel, I.Shareef, AA.Aliyu, Rate effects on delamination fracture toughness of a toughened graphite/epoxy, in: *Toughened composites*, ASTM International, 1987.
- [39] Y.-W. Mai, A. G. Atkins, R. M. Caddell, On the stability of cracking in tapered dcb testpieces, *International journal of fracture* 11 (1975) 939–953.
- [40] R. Heinzmann, R. Seghir, S.-Y. Alam, J. Réthoré, Experimental investigation of the alternate recurrence of quasi-static and dynamic crack propagation in PMMA., Vol. 242, Springer, 2023.

- [41] A. V. Vasudevan, Deciphering triangular fracture patterns in pmma: how crack fragments in mixed mode loading, Ph.D. thesis, Sorbonne université (2018).
- [42] T. Vincent-Dospital, R. Toussaint, S. Santucci, L. Vanel, D. Bonamy, L. Hattali, A. Cochard, E. G. Flekkøy, K. J. Måløy, How heat controls fracture: the thermodynamics of creeping and avalanching cracks, *Soft Matter* 16 (41) (2020) 9590–9602.
- [43] K. Ravi-Chandar, M. Balzano, On the mechanics and mechanisms of crack growth in polymeric materials, *Engineering fracture mechanics* 30 (5) (1988) 713–727.
- [44] M. Hattali, J. Barés, L. Ponson, D. Bonamy, Low velocity surface fracture patterns in brittle material: A newly evidenced mechanical instability, *Materials Science Forum* 706 (2012) 920–924.
- [45] A. A. Griffith, VI. the phenomena of rupture and flow in solids, *Philosophical transactions of the royal society of london. Series A, containing papers of a mathematical or physical character* 221 (582-593) (1921) 163–198.
- [46] W. Bradley, W. Cantwell, H. H. Kausch, Viscoelastic creep crack growth: a review of fracture mechanical analyses, *Mechanics of time-dependent materials* 1 (1997) 241–268.
- [47] M. H. Meliani, Z. Azari, G. Pluinage, Y. Matvienko, New approach for the t-stress estimation for specimens with a u-notch, CP2009, September (2009).

- [48] R. Gledhill, A. Kinloch, S. Yamini, R. Young, Relationship between mechanical properties of and crack propagation in epoxy resin adhesives, *Polymer* 19 (5) (1978) 574–582.
- [49] R. Gledhill, A. Kinloch, Mechanics of crack growth in epoxide resins, *Polymer Engineering & Science* 19 (2) (1979) 82–88.
- [50] B. Blackman, J. Dear, A. Kinloch, H. Macgillivray, Y. Wang, J. Williams, P. Yayla, The failure of fibre composites and adhesively bonded fibre composites under high rates of test: Part I mode I loading-experimental studies, *Journal of Materials Science* 30 (1995) 5885–5900.
- [51] F. Daghia, C. Cluzel, The climbing drum peel test: An alternative to the double cantilever beam for the determination of fracture toughness of monolithic laminates, *Composites Part A: Applied Science and Manufacturing* 78 (2015) 70–83.
- [52] S. Bandyopadhyay, Review of the microscopic and macroscopic aspects of fracture of unmodified and modified epoxy resins, *Materials Science and Engineering: A* 125 (2) (1990) 157–184.